

Modification of Cathode Surface for Sulfide Electrolyte-Based All-Solid-State Batteries Using Sulfurized LiNbO₃ Coating

Ha Young Ko, Jesik Park, Joo Young Lee, and Yong Joon Park*

All-solid-state batteries (ASSBs) with sulfide electrolytes are promising for next-generation battery systems owing to their superior safety and favorable electrochemical properties. However, interfacial instability between the oxide cathode and sulfide electrolyte induces undesirable side reactions, degrading cell performance. This study develops a sulfurized LiNbO₃ coating to stabilize this interface. While conventional LiNbO₃ coatings reduce interfacial side reactions, their limited compatibility with sulfide electrolytes, due to Li-ion chemical potential differences, hinders ion transport. The sulfurized LiNbO₃ coating improves compatibility, acting as a buffer that reduces the Li-ion potential gradient and enhances interfacial conductivity. The coating effectively suppresses side

reactions, lowering cathode degradation and interfacial resistance. A simple and cost-effective sulfur treatment process is used, where sulfur sublimation at 300 °C forms a sulfurized outer layer on the coating. Electrochemical evaluations of the coating reveal significant capacity, rate capability, and cyclic performance improvements over conventional LiNbO₃ coatings. These findings underscore sulfur treatment as an effective method for stabilizing interfaces and enabling smooth Li-ion transport, highlighting the advantages of the sulfurized LiNbO₃ coating method. Overall, sulfurized LiNbO₃ coatings offer scalable solutions to interfacial challenges in sulfide-based ASSBs, thereby promoting improved performance and commercialization of solid-state battery systems.

1. Introduction

Lithium-ion batteries (LIBs) have revolutionized energy storage and are integral to modern technology. With the advancing application of LIBs, addressing safety concerns is critical. Battery explosions and ignitions underscore the need for safer technologies. Furthermore, enhancing energy density remains a key challenge. Despite significant advancements, further miniaturization and increased energy storage remain priorities. Moreover, expanding the operational temperature range is imperative. Currently, LIBs face limitations in extreme temperature conditions, both excessively hot and cold, necessitating the development of batteries capable of functioning reliably across a broader temperature range.^[1–7] All-solid-state batteries (ASSBs) offer a promising solution to existing issues.^[8–17] Replacing flammable organic liquid electrolytes with inorganic solid-state electrolytes significantly reduces the risk of ignition and explosion.^[18–26] Moreover, utilizing Li metal or novel anodes enhances the energy storage capacity of batteries by minimizing anode volume and weight.^[27–29] Further improvements in battery pack design, packing density,

and the reduction of ancillary systems, such as battery management systems (BMS) and cooling systems, can further increase energy density. Additionally, ASSBs demonstrate stable performance over a wide temperature range due to the thermal resilience of solid electrolytes compared to conventional liquid electrolytes.^[30–33] Even at low temperatures, the reduction in ionic conductivity is less than that of liquid electrolytes, ensuring relatively reliable operation and performance in diverse applications and environments, including extreme temperatures, where traditional Li-ion batteries underperform.

A promising candidate for ASSBs is lithium thiophosphate-based sulfide electrolytes, which offer high ionic conductivity and excellent processability, enhancing their commercialization potential.^[34–36] However, interfacial instability between sulfide electrolytes and electrodes leads to detrimental side reactions, including ionic exchange through interdiffusion and electrolyte decomposition during cycling. This reduces the electrochemical performance of sulfide electrolyte-based ASSBs compared to that of commercialized LIBs.^[37–40] Additionally, owing to the volume change of the cathode during charge and discharge, contact instability with the electrolyte prevents stable interface formation. Coating the cathode surface with stable materials can effectively enhance interface stability between the sulfide electrolyte and the cathode.^[41–45] Stable oxides^[46–50] are primarily used as coating materials, significantly reducing interfacial side reactions. While oxide coatings improve interface stability, a disparity in Li⁺ chemical potential between sulfide electrolyte and oxide coating materials hinders smooth Li-ions transport.^[51–53]

This study proposes a novel sulfurized LiNbO₃ coating material developed through reaction with sublimated sulfur vapor, to enhance interfacial compatibility in ASSBs. Previous studies have

H. Y. Ko, Y. J. Park

Department of Advanced Materials Engineering

Graduate School Kyonggi University

154-42, Gwanggyosan-Ro, Yeongtong-Gu, Suwon-Si, Gyeonggi-Do 16227,

Republic of Korea

E-mail: yjpark2006@kyonggi.ac.kr

J. Park, J. Y. Lee

Advanced Battery Development Team 3

Hyundai Motor Company

Hwasung-si, Gyeonggi-do 18280, Republic of Korea

 Supporting information for this article is available on the WWW under <https://doi.org/10.1002/batt.202500188>

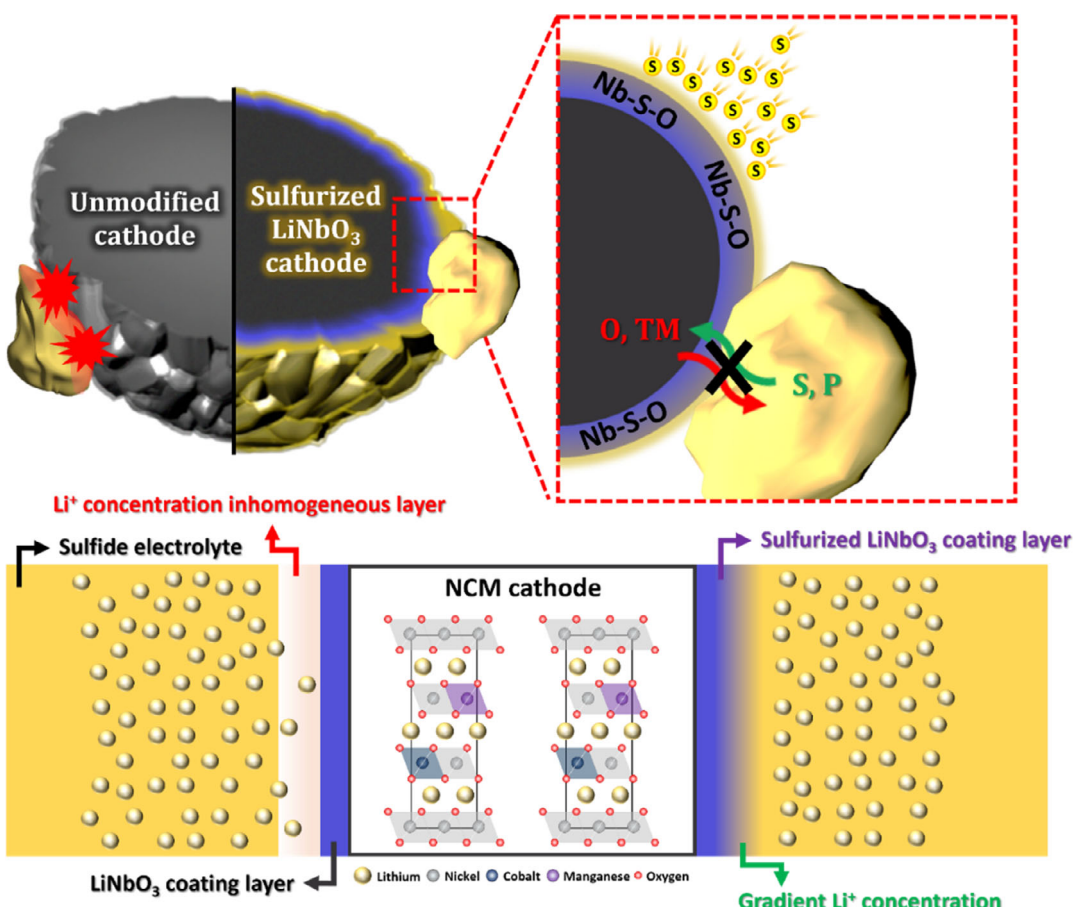


Figure 1. Schematic illustrating the effect of sulfurized LiNbO_3 coating layer on the surface of the cathode.

explored sulfur treatment to improve compatibility between sulfide electrolytes and coating materials.^[53] However, coating materials often formed mixed layers with sulfur-based materials rather than undergoing complete sulfurization. This study demonstrates the sulfurization of LiNbO_3 through sulfur treatment, enabling its function as an effective coating layer and interfacial stabilizer that enhances Li^+ ion conductivity. Figure 1 illustrates the schematic representation of sulfurized LiNbO_3 . Sulfurization of LiNbO_3 improves compatibility with the sulfide electrolyte, facilitating an effective buffer layer to reduce the Li^+ chemical potential difference between the cathode and electrolyte. The improved interface can facilitate smoother Li^+ transport and suppress interfacial side reactions. For experiments, high-Ni NCM ($\text{Li}[\text{Ni}_{0.82}\text{Co}_{0.1}\text{Mn}_{0.08}]_2\text{O}_2$) is used as the cathode material, and a range of analytical techniques are employed to thoroughly characterize the properties of the coating layer and assess its impact on interfacial stability. The results demonstrate the potential of sulfurized LiNbO_3 as an efficient interfacial stabilizer for ASSBs.

2. Results and Discussion

To evaluate the cathode characteristics of an all-solid-state cell with a LiNbO_3 coating, the electrochemical performance was analyzed under various coating conditions. Figure S1a, Supporting

Information, presents the initial charge-discharge profiles for a pristine NCM cathode (uncoated) and cathodes coated with 0.05, 0.1, and 0.15 wt% LiNbO_3 . At a current density of 8.5 mA g^{-1} , the pristine cathode exhibited a discharge capacity of $\approx 187 \text{ mAh g}^{-1}$, whereas the LiNbO_3 -coated cathodes displayed enhanced discharge capacities of $\approx 195 \text{ mAh g}^{-1}$ (0.05 and 0.1 wt%) and 201 mAh g^{-1} (0.15 wt%). Figure S1b, Supporting Information, shows a comparison of rate capabilities of these samples across increasing current densities (8.5, 17, 51, 85, and 170 mA g^{-1}), demonstrating that the LiNbO_3 -coated cathodes consistently outperformed the pristine cathode. Notably, while the 0.15 wt% LiNbO_3 coating exhibited the highest discharge capacity at 8.5 mA g^{-1} , its performance declined at elevated current densities relative to the 0.1 wt% LiNbO_3 coated cathode. Therefore, the 0.1 wt% LiNbO_3 coating was identified as the optimal condition, offering the best rate capability. A summary of discharge capacities is provided in Table S1, Supporting Information.

As a preliminary step prior to the sulfurization of the LiNbO_3 coating, a gas-phase sulfur treatment was applied to the pristine cathode surface, and its impact on electrochemical performance was evaluated. Figure S2, Supporting Information, illustrates the initial discharge capacity and rate capabilities of the cathodes subjected to sulfur treatment at sulfur concentrations of 500, 1000, 3000, and 5000 ppm (relative to cathode weight). The results revealed a significant enhancement in both discharge

capacity and rate capability following sulfurization, consistent with previous findings on cathodes of different compositions.^[53] A detailed comparison, provided in Table S2, Supporting Information, identified 1000 ppm as the optimal sulfur concentration, yielding the most substantial improvement in electrochemical performance.

The sulfurized LiNbO₃-coated cathode (hereafter referred to as the SLNO-cathode) was synthesized by applying a sulfur treatment (1000 ppm) to 0.1 wt% LiNbO₃-coated cathode (hereafter referred to as the LNO-cathode, determined as the optimal coating condition). A comparative analysis of the pristine, LNO, 1000 ppm sulfur-treated (without LiNbO₃ coating, referred to as sulfur-cathode), and SLNO-cathodes is presented in Figure 2. As shown in Figure 2a, the sulfur-cathode exhibited an initial discharge capacity of $\approx 198 \text{ mAh g}^{-1}$ at 8.5 mA g^{-1} , surpassing the performance of both the pristine and LNO-cathodes. At a high current density of 170 mA g^{-1} (Figure 2b), the sulfur-cathode maintained a higher discharge capacity ($\approx 138 \text{ mAh g}^{-1}$) compared to the LNO-cathode ($\approx 127 \text{ mAh g}^{-1}$), demonstrating the benefits of sulfur treatment. The SLNO-cathode exhibited an initial discharge capacity of $\approx 196 \text{ mAh g}^{-1}$, slightly lower than that of sulfur-cathode; however, at 170 mA g^{-1} , the SLNO-cathode achieved a remarkably higher discharge capacity of $\approx 149 \text{ mAh g}^{-1}$. A summary of discharge capacities and capacity retention is provided in Table 1. Capacity retention, calculated as the percentage of discharge capacity at 170 mA g^{-1} relative to 8.5 mA g^{-1} , was $\approx 54\%$ and 65% for the pristine and LNO-cathodes, respectively. The sulfur-cathode achieved a retention

of $\approx 70\%$, while the SLNO-cathode exhibited the highest retention of $\approx 76\%$. These findings demonstrate that sulfurization significantly enhances the effectiveness of the LiNbO₃ coating, particularly improving rate capability and high-current performance.

To investigate the characteristics of the coating layer, TEM analysis was performed. As shown in Figure 3, the surfaces of the pristine cathode (Figure 3a) and sulfur-cathode (Figure 3c) were smooth, with no distinct surface layers visible. Due to the characteristics of the high Ni NCM cathode, Li-residues were formed on the surface of the cathode. However, these residues were removed through washing and did not appear in the TEM images. Additionally, the layer formed during sulfur treatment may have been inadvertently removed during the washing process. Even without the washing step, observing the effects of sulfur treatment via TEM images was difficult because the sulfur-related layer was indistinguishable from the Li-residue. For the LNO (Figure 3b) and SLNO (Figure 3d) cathodes, a uniform coating layer of $\approx 2\text{--}3 \text{ nm}$ thickness was observed on the cathode surface. The coating layer uniformly covered the surface, and no apparent differences between the LNO and SLNO coating layers could be discerned in the TEM images.

Given the practical challenges of precisely analyzing the ultra-thin coating layer (2–3 nm) on the cathode surface, an in-depth analysis was conducted on LiNbO₃ powder synthesized using the same process as used for the coating layer fabrication. The process was followed by sulfurization under identical sulfur treatment conditions. Figure 4 presents the results of TOF-SIMS and XPS analyses performed on the sulfur-treated LiNbO₃ powder.

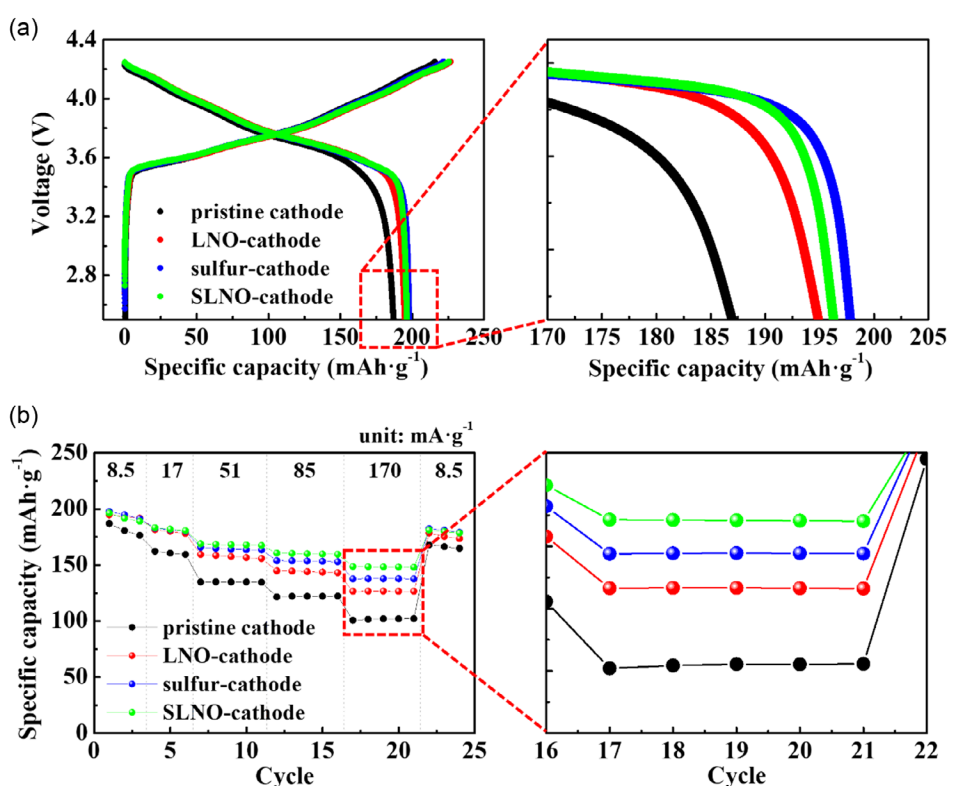


Figure 2. a) Initial charge–discharge curves at a current density of 8.5 mA g^{-1} and b) rate capabilities measured at $8.5, 17, 51, 85$, and 170 mA g^{-1} of pristine, LNO, sulfur, and SLNO cathodes.

Sample	Discharge capacity [mAh g^{-1}]					Capacity retention [% ^a]
	8.5 mA g^{-1} (1st cycle)	17 mA g^{-1} (4th cycle)	51 mA g^{-1} (7th cycle)	85 mA g^{-1} (12th cycle)	170 mA g^{-1} (17th cycle)	
Pristine cathode	187.0	162.3	134.8	121.5	100.9	53.9
LNO cathode	194.9	181.5	159.5	144.9	126.6	64.9
Sulfur cathode	197.8	182.9	165.7	154.0	137.6	69.6
SLNO cathode	196.3	183.3	169.0	160.6	148.6	75.7

^aCapacity retention is defined as the percentage of capacity maintained at 170 mA g^{-1} compared to that at 8.5 mA g^{-1} . Data in bold is the best performance.

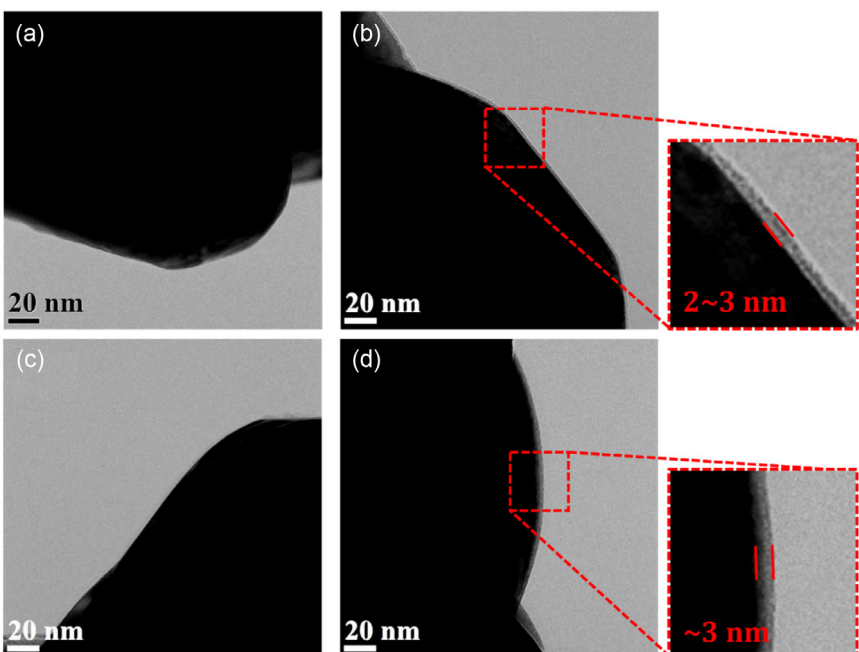


Figure 3. TEM images of a) pristine, b) LNO cathode, c) sulfur cathode, and d) SLNO cathode.

In the TOF-SIMS depth profile analysis prior to sulfur treatment (Figure 4a), strong signals for NbO^- ions were detected, while other elements were observed at background levels. Similarly, the XPS analysis (Figure 4b) revealed no discernible sulfur-related peaks before sulfurization. After sulfurization under 1000 ppm conditions—the same as those applied for the SLNO-cathode—the TOF-SIMS results presented a notable increase in the LiS^- and NbSO_3^- peaks on the surface (Figure 4c). The appearance of the LiS^- peak suggested the formation of Li-S compounds owing to the interaction between surface Li-residues and sulfur during treatment. Additional TOF-SIMS analysis for various sulfur oxide ions (SO_x) is summarized in Figure S3, Supporting Information. A significant increase in S^- , SO^- , SO_2^- , and SO_3^- ions was observed post-treatment. However, the increase in SO_4^- was relatively minimal. Notably, the pronounced intensity of the NbSO_3^- peak confirmed sulfurization via a chemical reaction between sulfur and LiNbO_3 , even at a relatively low temperature of 300 °C. Contrary to previous studies, where sulfur treatment of Li_3PO_4 coating resulted in no sulfurization,^[53] this study underscored the reactivity of LiNbO_3 under sulfur

treatment conditions. Furthermore, the XPS analysis (Figure 4d) corroborated these findings by displaying a clear increase in sulfur-related peaks (such as S^{4+} and S^{6+}). These results unequivocally demonstrated that sulfurization effectively occurred between LiNbO_3 and sulfur, forming a sulfurized LiNbO_3 layer.

To further elucidate the sulfurization behavior of LiNbO_3 , sulfur concentration was increased to 10 000 and 20 000 ppm, and the reactivity was closely analyzed. As shown in Figure 4e,g, the intensities of the LiS^- and NbSO_3^- peaks increased significantly with higher sulfur treatment levels. Correspondingly, as shown in Figure S3, Supporting Information, the results revealed that S^- along with SO^- , SO_2^- , and SO_3^- ions were detected in substantially greater quantities, indicating an active reaction where sulfur bonded with oxygen ions on the surface. Additionally, as presented in Figure S4, Supporting Information, the intensity of the NbSO_3^- peak consistently increased with higher sulfur treatment levels, further confirming the strong reactivity between LiNbO_3 and sulfur. This behavior was reflected in the XPS profiles shown in Figure 4f,h, where sulfur-related peak intensities continued to increase proportionally with sulfur concentrations.

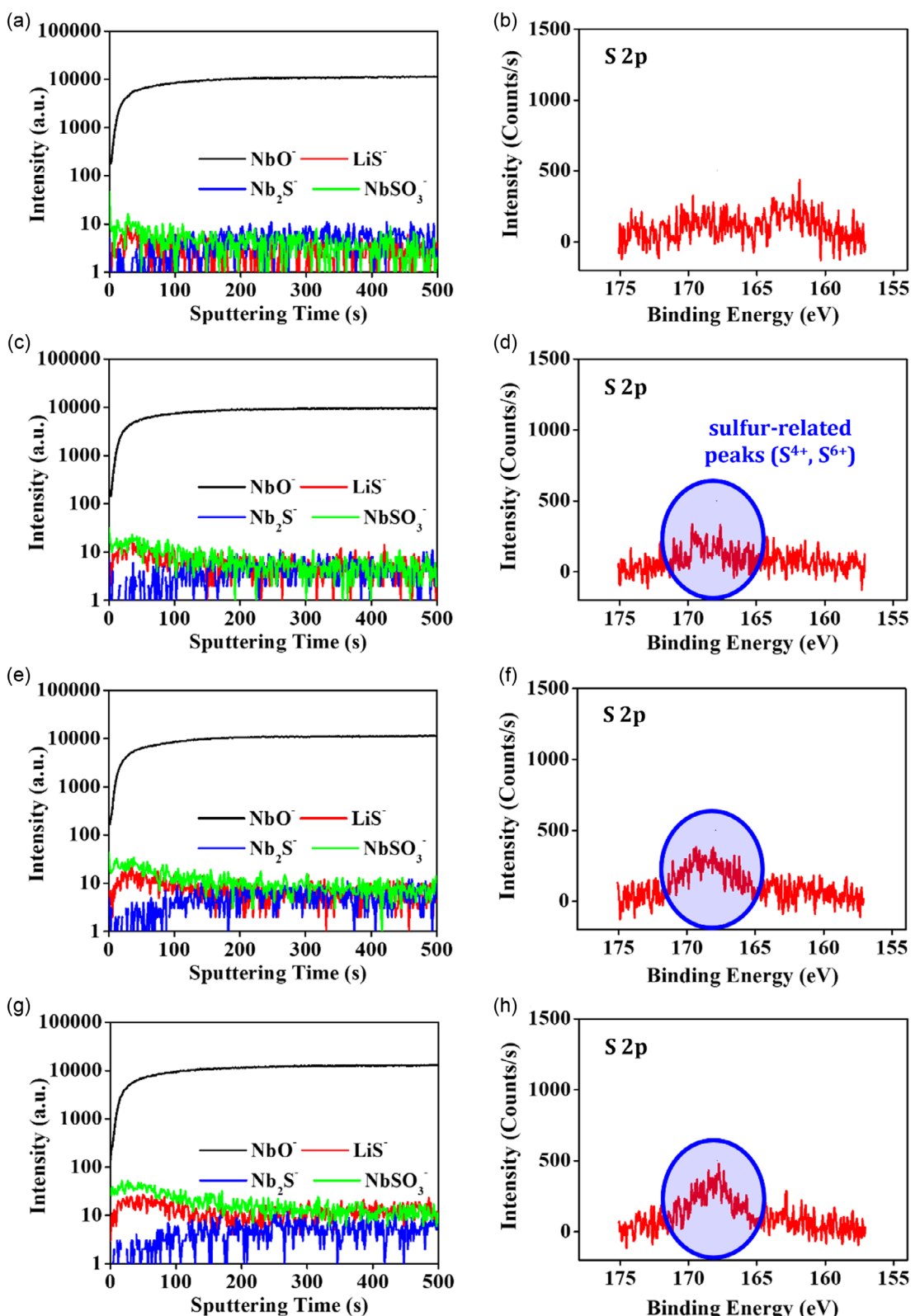


Figure 4. TOF SIMS image and XPS spectra of a,b) LiNbO_3 bulk powder, c,d) 1000 ppm sulfur-treated LiNbO_3 powder, e,f) 10 000 ppm sulfur-treated LiNbO_3 powder, and g,h) 20 000 ppm sulfur-treated LiNbO_3 powder.

Figure S5, Supporting Information, shows the fitting of the peaks in the $S\ 2p$ spectra. These results collectively demonstrated that the oxygen bonds in LiNbO_3 were relatively more reactive

with sulfur compared to the covalent PO_4^{3-} bonds in materials such as Li_3PO_4 . The heightened reactivity enabled sulfur to effectively bond with oxygen within the LiNbO_3 structure, facilitating

sulfurization even under moderate conditions. Notably, not all sulfur reacted directly with LiNbO₃. Based on the observed LiS⁻ and S⁻ peaks in the TOF-SIMS analysis, a considerable portion of sulfur interacted with Li-residue or existed as sulfide species on the surface. Nevertheless, the formation of sulfurized LiNbO₃, potentially containing byproducts such as LiS, was expected to function as an effective buffer layer. This buffer layer was particularly significant as it reduced the Li-ion potential mismatch between the cathode and the sulfide-based solid electrolyte, enhancing the overall performance of the all-solid-state cell.

Figure 5a illustrates the cycling performance of pristine, LNO-, and SLNO-cathodes over 300 cycles at 340 mA g⁻¹, with the corresponding discharge capacities at the 1st, 150th, and 300th cycles summarized in **Table 2**. The initial discharge capacity of the pristine cathode was \approx 144 mAh g⁻¹, while the LNO cathode exhibited a modest improvement to \approx 150 mAh g⁻¹. The SLNO cathode demonstrated an initial discharge capacity of \approx 149 mAh g⁻¹, comparable to the LNO cathode. During cycling, the surface-coated cathodes exhibited an enhancement in cyclic performance compared to the pristine cathode. Specifically, the pristine cathode exhibited a rapid decline in discharge capacity,

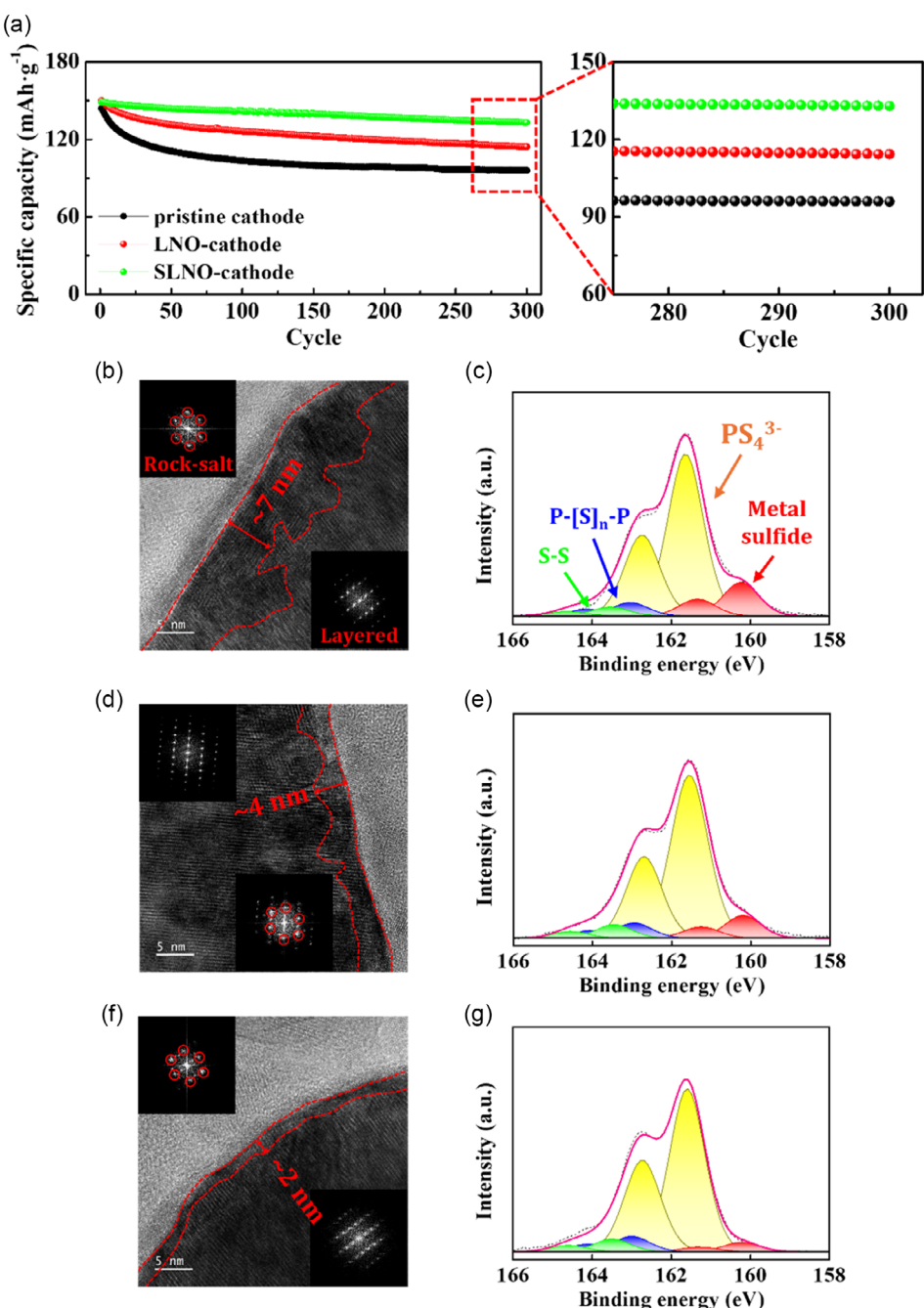


Figure 5. a) Cycling performance of pristine, LNO, and SLNO cathodes; TEM image and S 2p XPS spectra after 300 cycles for the b,c) pristine cathode, d,e) LNO-cathode, and f,g) SLNO-cathode.

Table 2. Discharge capacities at 1st, 150th, and 300th cycles and retained capacity after 300 cycles of the pristine, LNO, and SLNO cathodes (measured at 340 mA g⁻¹). Data in bold is the best performance.

Sample	Discharge capacity [mAh g ⁻¹]		Retained capacity after 300 cycles [%]	
	340 mA g ⁻¹			
	1st cycle	150th cycle		
Pristine cathode	144.1	99.9	66.6	
LNO cathode	150.1	122.6	76.1	
SLNO cathode	148.7	140.0	89.4	

retaining only \approx 96 mAh g⁻¹ after 300 cycles, corresponding to a retained capacity ratio (after 300 cycles) of \approx 66.6%. In contrast, the LNO cathode retained a discharge capacity of \approx 114 mAh g⁻¹ after 300 cycles, reflecting an improved retained capacity ratio of \approx 76.1% due to the protective effects of the LiNbO₃ coating layer. The improvement in cyclic performance was significantly pronounced in the SLNO cathode. After 300 cycles, the SLNO cathode retained a discharge capacity of \approx 133 mAh g⁻¹, representing a significantly higher retained capacity ratio of \approx 89.4%. These drastic improvements underscored the superior effectiveness of the sulfurized LiNbO₃ coating in reducing capacity degradation during long-term cycling. The enhanced cycling performance of the SLNO-cathode was attributed to its superior capability of suppressing side reactions at the cathode–electrolyte interface, which serves as a major cause of capacity fade in sulfide-based ASSBs. The sulfurized LiNbO₃ coating, along with sulfur-related reaction products such as LiS formed during the sulfur treatment process, played a pivotal role in further stabilizing the cathode–electrolyte interface and suppressing detrimental side reactions. This stabilizing capability significantly surpassed the performance achieved with a conventional LiNbO₃ coating only, as the sulfurization process introduced additional functionality to the coating layer, reinforcing its effectiveness in controlling side reactions and improving long-term cycling stability.

To investigate the role of surface coating in mitigating side reactions, a composite electrode was cycled 300 times and analyzed via TEM and XPS. Figure S6a, Supporting Information, presents a cross-sectional TEM image of the composite-electrode prior to cycling, demonstrating a well-preserved cathode surface with a distinct layered structure, as confirmed by spot patterns on the surface. As illustrated in Figure 5b, significant changes were observed after 300 cycles in the pristine cathode. A side-reaction layer formed on the surface. While the internal cathode retained its layered structure, the surface displayed a spot pattern indicative of a rock-salt structure. This transformation highlighted structural changes at the interface, resulting from ionic exchange during cycling. Specifically, sulfur and phosphorus ions from the sulfide electrolyte migrated into the cathode, while oxygen, nickel, cobalt, and manganese ions from the cathode diffused into the electrolyte.^[25–27] These interfacial changes led to the formation of a degraded surface layer, which hindered the transport of Li-ions and electrons. The changes damaged the surface and significantly affected the electrochemical performance of all-solid-state cells.

The occurrence of side reactions during cycling was further verified through XPS analysis. Figure S6b, Supporting Information,

illustrates the S 2p spectrum of the composite electrode before cycling. The dominant peaks at 161.6 and 162.7 eV corresponded to the PS₄³⁻ units within the sulfide electrolyte, as highlighted in yellow.^[36,54] Further, the red peaks at 160.2 and 161.4 eV were attributed to transition metal sulfides and lithium sulfide formed from ionic exchange between the cathode and electrolyte.^[28,53,55] Additionally, the blue peaks at 163.0 and 164.1 eV, along with the green peaks at 163.5 and 164.6 eV, were associated with reaction products formed by electrolyte decomposition, such as P-[S]_n-P bonds and S-S bonds.^[56,57] As depicted in Figure 5c, after 300 cycles, the intensity of the red peaks corresponding to sulfide reactants increased significantly. This increase underscored the active occurrence of side reactions at the cathode–electrolyte interface, driven by ionic exchange processes.

The LiNbO₃ coating exhibited significant efficacy in reducing side reactions. Figure 5d illustrates the TEM image of the composite electrode with the LNO cathode after 300 cycles, revealing a notably thinner damaged surface layer compared to the pristine cathode. Furthermore, the intensity of the red peaks associated with side reactions in the S 2p spectrum (Figure 5e) was markedly diminished compared to the spectrum of the pristine cathode (Figure 5c). However, the blue and green peaks related to electrolyte decomposition exhibited a slight increase. For the pristine cathode, active ionic exchange between the cathode and sulfide electrolyte enabled sulfur-related decomposition products to react with oxygen or transition metals in the cathode, forming sulfide reactants observed as red peaks in the XPS spectrum. Contrarily, the presence of the LiNbO₃ coating regulated ionic exchange, thereby limiting the formation of sulfide reactants and increasing the detection of electrolyte decomposition products, such as P-[S]_n-P bonds and S-S bonds, in the composite electrode. The TEM image of the composite electrode employing the SLNO-cathode after 300 cycles is presented in Figure 5f. Although a surface layer with a rock-salt structure was still observed, the extent of the damaged layer was reduced compared to the LNO cathode. In Figure 5g, the intensity of the red peaks, corresponding to sulfide reactants, was lower than that of the LNO-cathode, signifying a substantial reduction in by-product formation. Figure S7 and S8, Supporting Information, present a comparison of the damaged layer thickness observed in the TEM images and the intensity of the red peaks in the XPS spectra. These results underscored the effectiveness of sulfurized LiNbO₃ coating in suppressing side reactions and minimizing the formation of unwanted reaction products. This enhanced control over side reactions directly correlated with the superior electrochemical performance of the all-solid-state cells employing SLNO-cathodes, as shown in Figure 2 and 5a.

The sulfurization of LiNbO₃ was hypothesized to not only mitigate side reactions but also reduce the difference in Li-ion potential between the sulfide electrolyte and the oxide cathode, thereby facilitating smoother Li-ion transport across the interface. To validate the hypothesis, impedance analysis and Li-diffusion coefficients (D_{Li^+}) calculations were performed using the galvanostatic intermittent titration technique (GITT). Figure 6a–c presents the Nyquist plots of cells employing pristine, LNO, and SLNO cathodes after the 1st and 300th cycles, respectively. The semicircle in the Nyquist plots corresponded to the magnitude of the

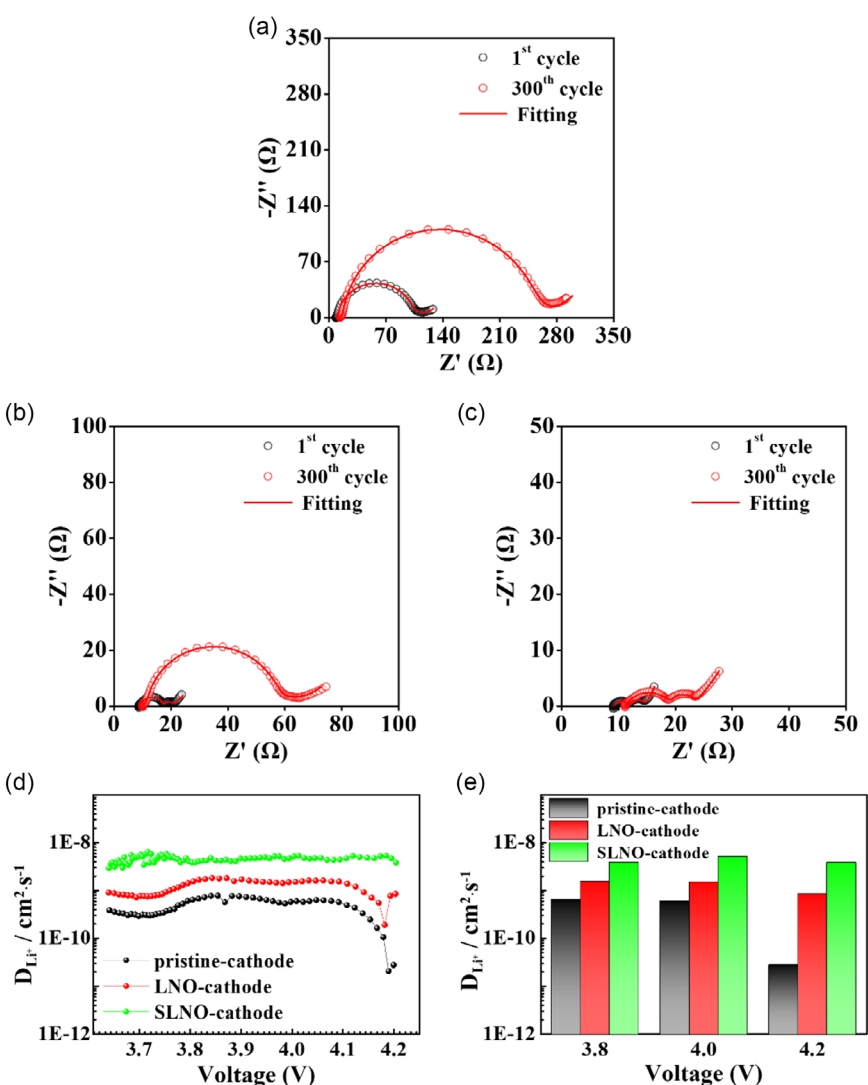


Figure 6. Nyquist plots of cells after 1st and 300th cycles containing a) pristine, b) LNO, and c) SLNO cathodes. d) Li-diffusion coefficients (D_{Li^+}) estimated from GITT curves measured after 300 cycles. e) Comparison of the D_{Li^+} values at 3.8, 4.0, and 4.2 V.

impedance resistance components. Notably, the resistive components of the LNO cathode were significantly smaller than those of the pristine cathode, indicating the beneficial effect of the LiNbO_3 coating in reducing interfacial resistance. Further, the resistive components were reduced in the SLNO-cathode, demonstrating the drastic effect of sulfurized LiNbO_3 in improving interfacial conductivity. To enable a more precise comparison, the Nyquist plots were fitted using the equivalent circuit shown in Figure S9, Supporting Information, and the impedance values

were extracted and summarized as shown in **Table 3**. While varying interpretations of the impedance components in all-solid-state cells have been presented in previous studies,^[43,46,54,58] the general consensus follows that the total impedance can be decomposed into the following contributions: bulk resistance of the solid electrolyte (R_b), grain-boundary resistance of the solid electrolyte (R_G), cathode/solid electrolyte interfacial resistance ($R_{C/S}$), and anode/solid electrolyte interfacial resistance ($R_{A/S}$).^[54,58]

Table 3. Impedance values calculated from the Nyquist plots of the cells containing pristine, LNO, and SLNO cathodes. Bold indicates the impedance values of $R_{C/S}$, representing the cathode/electrolyte interfacial resistance (the main focus of this study) are compared and emphasized.

Sample	After 1st cycle					After 300th cycle				
	R_b [Ω]	R_G [Ω]	$R_{C/S}$ [Ω]	$R_{A/S}$ [Ω]	R_{total} [Ω]	R_b [Ω]	R_G [Ω]	$R_{C/S}$ [Ω]	$R_{A/S}$ [Ω]	R_{total} [Ω]
Pristine cathode	8.9	1.0	95.9	4.4	110.2	13.8	1.4	242.5	9.6	267.3
LNO cathode	8.8	0.7	8.2	3.6	21.3	10.1	0.9	43.9	6.7	61.6
SLNO cathode	8.8	0.4	1.7	2.8	13.7	11.3	0.9	6.8	4.8	23.8

The interfacial resistance ($R_{c/s}$) demonstrated the impact of surface coatings on the impedance characteristics of the cells. For the pristine cathode, $R_{c/s}$ was measured at $95.9\ \Omega$ after the first cycle and escalated drastically to $\approx 242.5\ \Omega$ after the 300th cycle, highlighting substantial interfacial degradation due to uncontrolled side reactions. Contrarily, the application of a LiNbO₃ coating (LNO cathode) significantly reduced $R_{c/s}$ to ≈ 8.2 and $43.9\ \Omega$ after the first and 300th cycles, respectively, underscoring the effectiveness of the coating in reducing interfacial side reactions and stabilizing the interface. The effect was highly pronounced when sulfurized LiNbO₃ coating was used. The $R_{c/s}$ of the SLNO-cathode cell reduced to $1.7\ \Omega$ after the first cycle and to $6.8\ \Omega$ after the 300th cycle. Therefore, the sulfurized LiNbO₃ coating, along with sulfur-related residues formed during the sulfurization process, significantly enhanced interfacial stability.

Figure 6d presents the Li-ion diffusion coefficient (D_{Li^+}) of pristine, LNO, and SLNO cathodes after 300 cycles for 3.64–4.2 V. The full GITT voltage profiles used for the measurements are shown in Figure S10, Supporting Information. The results indicated that both LNO and SLNO cathodes exhibited enhanced D_{Li^+} values compared to the pristine cathode, with the SLNO cathode demonstrating the most significant improvement. Figure 6e presents a comparison of the D_{Li^+} values at 3.8, 4.0, and 4.2 V, revealing that the effect of surface coating grew increasingly pronounced at higher voltages. The observed enhancement in Li-ion diffusivity with LiNbO₃ coating was attributed to its ability to mitigate the formation of undesirable side reaction layers at the cathode–electrolyte interface, thereby facilitating Li-ion transport. Additionally, the incorporation of sulfur into the LiNbO₃ layer improved the chemical compatibility between the interface protection layer and the sulfide-based solid electrolyte. This enhanced interfacial stability further promoted Li-ion transport kinetics, leading to a superior D_{Li^+} value in SLNO-coated cathodes compared to LNO-coated ones. The improved Li-ion diffusion properties of SLNO-coated cathodes directly correlated with the superior rate capability of all-solid-state cells, as presented in Figure 2b. These findings underscored the potential of sulfurized LiNbO₃ as an effective surface modification strategy for enhancing the electrochemical performance of next-generation all-solid-state batteries.

3. Conclusion

This study introduces sulfurized LiNbO₃ coatings as an effective strategy to suppress undesirable side reactions between the sulfide electrolyte and cathode while enhancing Li-ion transport across the interface. Although conventional LiNbO₃ coatings are well-established for their role in stabilizing the interface and improving electrochemical performance, the sulfurized LiNbO₃ coating—synthesized via a cost-effective gas-phase reaction using sulfur sublimation at $300\ ^\circ\text{C}$ —demonstrates superior functionality as a cathode coating material. The application of LiNbO₃ coatings results in notable improvements in capacity, rate capability, and cyclic stability compared to pristine cathodes. However, sulfurized LiNbO₃-coated cathodes exhibit greater enhancements in electrochemical performance, underscoring the effectiveness of sulfurization. Despite the absence of

discernible structural changes in the coating layer via TEM imaging, advanced characterization techniques such as TOF-SIMS and XPS confirm the successful sulfurization of LiNbO₃. The analyses reveal a reaction between the outer surface of the LiNbO₃ coating layer and sulfur, along with the formation of sulfurized LiNbO₃ and sulfur-related compounds such as LiS, SO₂, and LiSO_x. These residues, formed during the sulfur treatment process, play a critical role in suppressing interfacial side reactions and facilitating ion transport. Postcycling analysis via cross-sectional TEM and XPS validate the findings, revealing that while LiNbO₃ coatings effectively limit undesired interfacial degradation, sulfurized LiNbO₃ coatings achieve greater suppression of undesired interfacial layer formation. Impedance spectroscopy and GITT measurements corroborate these observations, demonstrating that sulfurized LiNbO₃ coatings substantially reduce interfacial resistance ($R_{c/s}$) and improve Li-ion conductivity. These enhancements directly contribute to superior electrochemical performance, including enhanced capacity retention and long-term cycling stability. This study highlights the critical role of sulfurization in improving cathode–sulfide electrolyte compatibility, which is essential for minimizing interfacial resistance and promoting Li-ion mobility. The simplicity, cost-effectiveness, and scalability of the sulfurized LiNbO₃ coating process position it as a promising strategy for advancing ASSB technology. Furthermore, the methodology developed in this study has applicability, offering new avenues for optimizing interface engineering to enhance stability and efficiency of ASSBs.

4. Experimental Section

The Li[Ni_{0.82}Co_{0.1}Mn_{0.08}]O₂ powder, supplied by Hyundai Motors, was used as the pristine cathode material. The LiNbO₃ coating solution was prepared by dissolving niobium pentaethoxide (Nb(OC₂H₅)₅, 99.99%, Kojundo Chemical Laboratory Co., Ltd.) and lithium ethoxide (LiOC₂H₅, 99.9%, Kojundo Chemical Laboratory Co., Ltd.) in anhydrous ethanol (CH₃CH₂OH, Sigma–Aldrich). The LiNbO₃ coating was applied at concentrations of 0.05, 0.1, and 0.15 wt% relative to the pristine cathode material. The coating process involved mixing the cathode powder with the prepared solution, followed by continuous stirring at $70\ ^\circ\text{C}$ until complete solvent evaporation. The resulting mixture was dried under vacuum at $90\ ^\circ\text{C}$ for 2 h and subsequently annealed at $600\ ^\circ\text{C}$ for 5 h in an oxygen atmosphere to obtain the LiNbO₃-coated cathode material. Sulfurization was performed on both the pristine and 0.1 wt% LiNbO₃-coated cathodes. Solid sulfur (S flakes, 99.998% trace metals basis, Sigma–Aldrich) was used as the sulfur source and mechanically ground with zirconia balls in a 1:1 volume ratio at 30 Hz for 5 min. The ground sulfur was sieved using a 38 μm mesh to obtain fine sulfur powder, which was then mixed with the cathode materials at sulfur concentrations of 500, 1000, 3000, and 5000 ppm. The mixture was homogenized by mechanical mixing at 30 Hz for 3 min and subsequently heat-treated in a sealed tube under an argon atmosphere at $300\ ^\circ\text{C}$ for 4 h.

The formation of the coating layer on both pristine and surface-modified cathodes was confirmed using transmission electron microscopy (TEM, JEOL JEM-2100F). To further analyze the ultrathin coating, LiNbO₃ powder was synthesized following the same procedure as that for coating layer formation and subsequently sulfurized at concentrations of 1000, 10 000, and 20 000 ppm. Time-of-flight secondary-ion mass spectrometry (TOF-SIMS, TOFSIMS.5, Bi⁺) and X-ray photoelectron spectroscopy (XPS, ThermoFisher Scientific NEXSA) were employed to investigate the extent of sulfurization in LiNbO₃ powder and identify the resulting ionic species. To evaluate the electrochemical effect of sulfurized LiNbO₃, ASSBs were

assembled using a pressurized cell configuration. The composite cathode was prepared by mixing the active material, sulfide solid electrolyte ($\text{Li}_6\text{PS}_5\text{Cl}$, supplied by Hyundai Motors), and a conductive additive (Super-C, supplied by Hyundai Motors) in a weight ratio of 70:30:2, followed by manual mixing in an agate mortar. The solid electrolyte (0.15 g) was initially compressed at 12 MPa, followed by the addition of composite cathode (0.015 g) and further compression at 44 MPa. An aluminum foil current collector was positioned on the composite cathode layer, while lithium metal foil served as the anode. The final cathode/electrolyte/anode pellet was assembled under a pressure of 50 kgf cm using a torque wrench. To prevent exposure to oxygen and moisture, all assembly steps were conducted in a high-purity argon-filled glove box. Electrochemical performance tests were conducted at 30 °C within a voltage range of 2.5–4.25 V (versus Li).

To assess structural changes at the cathode surface after 300 charge–discharge cycles, focused ion beam (FIB, Quanta 3D FEG) was used to prepare cross-sectional samples of the composite electrode. These cross-sections were analyzed via TEM (Titan TM 80-300), with a vacuum transfer TEM holder employed to minimize undesired reactions during sample preparation. X-ray photoelectron spectroscopy (XPS, K-alpha⁺) was conducted to examine the elemental composition and chemical states at the cathode/electrolyte interface after prolonged cycling. Electrochemical impedance spectroscopy (EIS, AMETEK, VersaSTAT 3) was performed to evaluate the impedance characteristics of cells. Measurements were conducted on fully charged cells after 300 cycles using an alternating voltage amplitude of 10 mV over a frequency range of 0.01 Hz to 500 kHz. The resulting Nyquist plots were analyzed and fitted using ZSimpWin 3.60 software. The Li^+ diffusion characteristics following charge–discharge cycling were assessed using the galvanostatic intermittent titration technique (GITT). A pulse current of 0.1C was applied intermittently for 10 min, followed by a relaxation period to allow the system to reach equilibrium. The Li^+ diffusion coefficient (D_{Li^+}) was determined using Equation (1).

$$D_{\text{Li}^+} = \frac{4}{\pi\tau} \left(\frac{n_m V_m}{S} \right)^2 \left(\frac{\Delta E_s}{\Delta E_t} \right)^2 \quad (1)$$

where τ represents the pulse duration (600 s). n_m is the number of moles. V_m is the molar volume of the active material, and S corresponds to the contact area between the solid electrolyte and composite electrode. Here, ΔE_t and ΔE_s denote the transient and steady-state voltage changes, respectively.

Acknowledgements

This study was supported by a National Research Foundation of Korea (NRF) grant funded by the Korean government (no. RS-2023-NR076421) and Hyundai NGV. This work was also supported by the Materials and Components Technology Development Program (grant no. 20024249) and Technology Innovation Program (grant no. 00427225) funded by the Ministry of Trade, Industry & Energy (MOTIE, Korea).

Conflict of Interest

The authors declare no conflict of interest.

Data Availability Statement

The data that support the findings of this study are available in the supplementary material of this article.

Keywords: all solid state batteries • cathodes • sulfurization • surface modification

- [1] Y. Chen, Y. Kang, Y. Zhao, L. Wang, J. Liu, Y. Li, Z. Liang, X. He, X. Li, N. Tavajohi, B. Li, *J. Energy Chem.* **2021**, *59*, 83.
- [2] L. Wu, *Electrochim. Energy Rev.* **2021**, *4*, 101.
- [3] C. Heubner, K. Nikolowski, S. Reuber, M. Schneider, M. Wolter, A. Michaelis, *Batteries Supercaps* **2021**, *4*, 268.
- [4] X. Zhou, S. Li, Z. Feng, S. Zhang, X. Fan, Y. Wang, D. Sun, H. Li, Y. Tang, H. Wang, J. Li, J. Wei, *Batteries Supercaps* **2023**, *6*, e202300229.
- [5] S. H. Kwak, Y. J. Park, *Batteries* **2024**, *10*, 348.
- [6] Z. Meng, J. Hou, P. Thanwisai, J. Fu, Z. Yao, Y. Zheng, W. Jin, Z. Wang, Z. Yang, X. Ma, Y. Wang, *Batteries Supercaps* **2024**, *7*, e202400107.
- [7] H. J. Im, Y. J. Park, *ACS Appl. Mater. Interfaces* **2022**, *14*, 38952.
- [8] J. Wu, S. Liu, F. Han, X. Yao, C. Wang, *Adv. Mater.* **2021**, *33*, 2000751.
- [9] G. Peng, X. Yao, H. Wan, B. Huang, J. Yin, F. Ding, X. Xu, *J. Power Sources* **2016**, *307*, 724.
- [10] J. Yin, X. Yao, G. Peng, J. Yang, Z. Huang, D. Liu, Y. Tao, X. Xu, *Solid State Ionics* **2015**, *274*, 8.
- [11] Y. Liang, H. Liu, G. Wang, C. Wang, Y. Ni, C. W. Nan, L. Z. Fan, *InfoMat* **2022**, *4*, 1.
- [12] K. Wang, Z. Liang, S. Weng, Y. Ding, Y. Su, Y. Wu, H. Zhong, A. Fu, Y. Sun, M. Luo, J. Yan, X. Wang, Y. Yang, *ACS Energy Lett.* **2023**, *8*, 3450.
- [13] M. Ma, M. Zhang, B. Jiang, Y. Du, B. Hu, C. Sun, *Mater. Chem. Front.* **2023**, *7*, 1268.
- [14] C. Li, Z. Y. Wang, Z.-J. He, Y. J. Li, J. Mao, K.-H. Dai, C. Yan, J. C. Zheng, *Sustainable Mater. Technol.* **2021**, *29*, e00297.
- [15] Z. Ding, J. Li, J. Li, C. An, *J. Electrochim. Soc.* **2020**, *167*, 070541.
- [16] Z. Gao, H. Sun, L. Fu, F. Ye, Y. Zhang, W. Luo, Y. Huang, *Adv. Mater.* **2018**, *30*, 1705702.
- [17] Y. Kato, S. Hori, T. Saito, K. Suzuki, M. Hirayama, A. Mitsui, M. Yonemura, H. Iba, R. Kanno, *Nat. Energy* **2016**, *1*, 1.
- [18] L. Fan, H. He, C. Nan, *Nat. Rev. Mater.* **2021**, *6*, 1003.
- [19] H. Liu, Y. Liang, C. Wang, D. Li, X. Yan, C. Nan, *Adv. Mater.* **2023**, *35*, 2206013.
- [20] D. Li, X. Liu, Y. Li, X. Zhao, M. Wu, X. Qi, L. Gao, L. Fan, *Energy Mater.* **2024**, *14*, 2402929.
- [21] L. Li, W. Zhang, J. Zhang, J. Ren, X. Guo, X. Lu, *Energy Storage Mater.* **2025**, *77*, 104224.
- [22] X. Qi, G. Wu, M. Wu, D. Li, C. Wang, L. Gao, S. Zhang, L. Fan, *J. Energy Chem.* **2025**, *103*, 926.
- [23] D. Li, H. Liu, C. Wang, C. Yan, Q. Zhang, C. Nan, L. Fan, *Adv. Funct. Mater.* **2024**, *34*, 2315555.
- [24] Y. Liang, X. Zhu, X. Fan, D. Li, F. Xu, H. Yu, L. Fan, *Chem. Eng. J.* **2024**, *485*, 149575.
- [25] W. G. Suci, H. Kasuma, K. Aliwarga, Y. R. Azinuddin, *Open Eng.* **2022**, *12*, 409.
- [26] C. Wang, J. Liang, Y. Zhao, M. Zheng, X. Li, X. Sun, *Energy Environ. Sci.* **2021**, *14*, 2577.
- [27] L. Xu, S. Tang, Y. Cheng, K. Wang, J. Liang, C. Liu, Y. C. Cao, F. Wei, L. Mai, *Joule* **2018**, *2*, 1991.
- [28] Y. Lee, S. Fujiki, C. Jung, N. Suzuki, N. Yashiro, R. Omoda, D. Ko, T. Shiratsuchi, T. Sugimoto, S. Ryu, J. H. Ku, T. Watanabe, Y. Park, Y. Aihara, D. Im, I. T. Han, *Nat. Energy* **2020**, *5*, 299.
- [29] D. H. S. Tan, Y. T. Chen, H. Yang, W. Bao, B. Sreenarayanan, J. M. Doux, W. Li, B. Lu, S. Y. Ham, B. Sayahpour, J. Scharf, E. A. Wu, G. Deysher, H. E. Han, H. J. Hah, H. Jeong, J. B. Lee, Z. Chen, Y. S. Meng, *Science* **2021**, *373*, 1494.
- [30] Y. K. Sun, *ACS Energy Lett.* **2020**, *5*, 3221.
- [31] Y. Zheng, Y. Yao, J. Ou, M. Li, D. Luo, H. Dou, Z. Li, K. Amine, A. Yu, Z. Chen, *Chem. Soc. Rev.* **2020**, *49*, 8790.
- [32] L. Peng, C. Yu, Z. Zhang, R. Xu, M. Sun, L. Zhang, S. Cheng, J. Xie, *Energy Environ. Mater.* **2023**, *6*, e12308.
- [33] C. Sun, J. Liu, Y. Gong, D. P. Wilkinson, J. Zhang, *Nano Energy* **2017**, *33*, 363.
- [34] Q. Wu, S. Xiong, F. Li, A. Matic, *Batteries Supercaps* **2023**, *6*, e202300321.
- [35] S. Wang, R. Fang, Y. Li, Y. Liu, C. Xin, F. H. Richter, C. W. Nan, *J. Mater.* **2021**, *7*, 209.
- [36] Y. W. Byeon, H. Kim, *Electrochim* **2021**, *2*, 452.
- [37] J. Auvergniot, A. Cassel, J. B. Ledueil, V. Viallet, V. Seznec, R. Dedryvère, *Chem. Mater.* **2017**, *29*, 3883.
- [38] R. J. Chen, Y. B. Zhang, T. Liu, B. Q. Xu, Y. H. Lin, C. W. Nan, Y. Shen, *ACS Appl. Mater. Interfaces* **2017**, *9*, 9654.

- [39] A. Banerjee, H. Tang, X. Wang, J. H. Cheng, H. Nguyen, M. Zhang, D. H. S. Tan, T. A. Wynn, E. A. Wu, J. M. Doux, T. Wu, L. Ma, G. E. Sterbinsky, M. S. D'Souza, S. P. Ong, Y. S. Meng, *ACS Appl. Mater. Interfaces* **2019**, *11*, 43138.
- [40] R. Koerver, I. Aygün, T. Leichtweiß, C. Dietrich, W. Zhang, J. O. Binder, P. Hartmann, W. G. Zeier, J. Janek, *Chem. Mater.* **2017**, *29*, 5574.
- [41] K. Min, S. W. Seo, B. Choi, K. Park, E. Cho, *ACS Appl. Mater. Interfaces* **2017**, *9*, 17822.
- [42] D. H. Yoon, Y. J. Park, *Appl. Energy* **2022**, *326*, 119991.
- [43] A. Banerjee, X. Wang, C. Fang, E. A. Wu, Y. S. Meng, *Chem. Rev.* **2020**, *120*, 6878.
- [44] Y. Xiao, L. J. Miara, Y. Wang, G. Ceder, *Joule* **2019**, *3*, 1252.
- [45] Y. J. Park, Y. Su, K. Yamamoto, T. Watanabe, N. Thakur, M. Kumar, T. Matsunaga, Y. Uchimoto, *Batteries Supercaps* **2025**, e202400697.
- [46] X. Li, L. Jin, D. Song, H. Zhang, X. Shi, Z. Wang, L. Zhang, L. Zhu, *J. Energy Chem.* **2020**, *40*, 39.
- [47] F. Walther, F. Strauss, X. Wu, B. Mogwitz, J. Hertle, J. Sann, M. Rohnke, T. Brezesinski, J. Janek, *Chem. Mater.* **2021**, *33*, 2110.
- [48] C. B. Lim, Y. J. Park, *Sci. Rep.* **2020**, *10*, 10501.
- [49] F. Strauss, J. H. Teo, J. Maibach, A. Y. Kim, A. Mazilkin, J. Janek, T. Brezesinski, *ACS Appl. Mater. Interfaces* **2020**, *12*, 57146.
- [50] J. S. Lee, Y. J. Park, *ACS Appl. Mater. Interfaces* **2021**, *13*, 38333.
- [51] J. Haruyama, K. Sodeyama, L. Han, K. Takada, Y. Tateyama, *Chem. Mater.* **2014**, *26*, 4248.
- [52] J. Liang, Y. Zhu, X. Li, J. Luo, S. Deng, Y. Zhao, Y. Sun, D. Wu, Y. Hu, W. Li, T. K. Sham, R. Li, M. Gu, X. Sun, *Nat. Commun.* **2023**, *14*, 146.
- [53] D. I. Jang, H. Y. Ko, J. Park, J. Y. Lee, Y. J. Park, *ACS Energy Lett.* **2024**, *9*, 5966.
- [54] A. Y. Kim, F. Strauss, T. Bartsch, J. H. Teo, T. Hatsukade, A. Mazilkin, J. Janek, P. Hartmann, T. Brezesinski, *Chem. Mater.* **2019**, *31*, 9664.
- [55] Y. Xiao, Y. Wang, S. H. Bo, J. C. Kim, L. J. Miara, G. Ceder, *Nat. Rev. Mater.* **2020**, *5*, 105.
- [56] W. Zhang, T. Leichtweiß, S. P. Culver, R. Koerver, D. Das, D. A. Weber, W. G. Zeier, J. Janek, *ACS Appl. Mater. Interfaces* **2017**, *9*, 35888.
- [57] M. J. Joo, M. Kim, S. Chae, M. Ko, Y. J. Park, *ACS Appl. Mater. Interfaces* **2023**, *15*, 59389.
- [58] P. Vadhma, J. Hu, M. J. Johnson, R. Stocker, M. Braglia, D. J. L. Brett, A. J. E. Rettie, *ChemElectroChem* **2021**, *8*, 1930.

Manuscript received: March 14, 2025

Revised manuscript received: May 23, 2025

Version of record online: